Journal of Power Sources 338 (2017) 49–64

Contents lists available at ScienceDirect

Journal of Power Sources

journal homepage: www.elsevier.com/locate/jpowsour

Plug-in hybrid electric vehicle $LiFePO_4$ battery life implications of thermal management, driving conditions, and regional climate

Tugce Yuksel [a], Shawn Litster [b], Venkatasubramanian Viswanathan [b], Jeremy J. Michalek [b, c, *]

[a] Faculty of Engineering and Natural Sciences, Sabanci University, Istanbul, 34956 Tuzla, Istanbul, Turkey
[b] Department of Mechanical Engineering, Carnegie Mellon University, Pittsburgh, PA 15213, USA
[c] Department of Engineering and Public Policy, Carnegie Mellon University, Pittsburgh, PA 15213, USA

HIGHLIGHTS

- Comprehensive simulation model of a PHEV battery with LFP cells.
- Without cooling, aggressive driving can cut battery life by 2/3 in hot regions.
- Batteries last 73–94% longer in mild-weather regions than hot regions.
- Air cooling can increase life by a factor of 1.5–6.
- Results are sensitive to end of life criteria.

ARTICLE INFO

Article history:
Received 15 June 2016
Received in revised form
14 October 2016
Accepted 29 October 2016
Available online 15 November 2016

Keywords:
Battery life
Battery degradation
Plug-in hybrid electric vehicle
Thermal management
Lithium-ion

ABSTRACT

Battery degradation strongly depends on temperature, and many plug-in electric vehicle applications employ thermal management strategies to extend battery life. The effectiveness of thermal management depends on the design of the thermal management system as well as the battery chemistry, cell and pack design, vehicle system characteristics, and operating conditions. We model a plug-in hybrid electric vehicle with an air-cooled battery pack composed of cylindrical $LiFePO_4$/graphite cells and simulate the effect of thermal management, driving conditions, regional climate, and vehicle system design on battery life. We estimate that in the absence of thermal management, aggressive driving can cut battery life by two thirds; a blended gas/electric-operation control strategy can quadruple battery life relative to an all-electric control strategy; larger battery packs can extend life by an order of magnitude relative to small packs used for all-electric operation; and batteries last 73–94% longer in mild-weather San Francisco than in hot Phoenix. Air cooling can increase battery life by a factor of 1.5–6, depending on regional climate and driving patterns. End of life criteria has a substantial effect on battery life estimates.

1. Introduction

Plug-in electric vehicles (PEVs) have the potential to reduce operating cost, greenhouse gas (GHG) emissions, and petroleum consumption [1,2], but high battery cost is a significant barrier to PEV adoption [1,3–5]. For many PEVs, the battery is the most expensive component of the vehicle [6], so if the battery fails to last the life of the vehicle, battery replacement can significantly harm PEV cost competitiveness. The battery industry traditionally defines end-of-life (EOL) as the point where the battery's energy storage capacity drops by 20% of its initial value or when 30% internal impedance growth is reached, whichever comes first [7]; however, different vehicle design criteria can imply different EOL criteria [8].

Battery life is usually characterized in terms of cycle life and calendar life. Cycle life is the number of complete discharge and charge cycles that can be expected from the battery before it reaches its EOL criteria – a measure of battery life during active use. In contrast, calendar life is the time it takes for a battery to reach the EOL criteria under standby (or storage) conditions [9]. According to the goals set by US Advanced Battery Consortium (USABC), a plug-

* Corresponding author. Department of Mechanical Engineering and Department of Engineering and Public Policy, Carnegie Mellon University, Pittsburgh, PA 15213, USA.
E-mail address: jmichalek@cmu.edu (J.J. Michalek).

http://dx.doi.org/10.1016/j.jpowsour.2016.10.104
0378-7753/

Table 1
LFP cycling fade studies reviewed.

	Cell description	Temp [°C]	C-rate	Fade per cycle (n) or Ah	DOD [%]	Cap. Fade	Imp. Growth
A123 Datasheet [25]	A123 26650 2.3 Ah	25,45,60	**Discharge:** 1C,2.2C, **Charge:** 1C,1.3C	n	N/A	Yes	No
Wang et al. [20]	A123 26650 2.3 Ah (paper says 2.2 Ah)	15,45,60[a]	C/2,2C, 6C, 10C[b]	Ah	10,50,80,90[c]	Yes	No
Peterson et al. [19]	A123 26650 2.3 Ah	~25	Simulated drive cycles	both	Drive cycles corresponding to DODs between 34 and 97%	Yes	No
Omar et al. [26]	2.3 Ah, 3.3 V No brand mentioned	−18,0,25,40	**Discharge:** 1C,5C, 10C,15C **Charge:** 0.25C,0.5C, 1C,2C,4C	n	20,40,60,80,100	Yes	Yes[d]
Song et al. [27]	1.2 Ah 18650 No brand	25,55	N/A	n	N/A	Yes	No
Li et al. [28]	11 Ah	30, 45	**Discharge:** 1/3C,4C **Charge:** 1/3C, 1.5C	n	N/A	Yes	No
Zhang et al. [14]	16.4 Ah No brand	−10,0, 25,45	UDDS	n[e]	N/A	Yes	Yes
Groot et al. [18]	A123 26650 2.3 Ah	Between 23 and 53	**Discharge:** 1C,2C,3.75C,4C **Charge:** 1C,2C,3.75C,4C	Ah	60%,100%	Yes	Yes

[a] It is mentioned that tests were performed at 0 °C and 25 °C as well, however test results are not reported in the paper.
[b] Data provided only for C/2, models provided for other C-rates.
[c] Not enough data for DOD dependence; it appears to matter at high C-rates, but the model does not include DOD dependence.
[d] There was actually quite significant resistance growth, but capacity fade was always faster, so no model is provided for impedance growth.
[e] Capacity fade and impedance growth are measured after 300 and 600 cycles only.

in hybrid electric vehicle (PHEV) battery is targeted to have 15 years of calendar life and 5000 cycles of charge depleting, 300,000 cycles of charge sustaining mode cycle life by 2018 [10,11].

Batteries degrade with time and usage, and degradation depends on the inherent characteristics of the battery such as its materials and design. Currently, PEVs use Li-ion batteries due to superior power and energy characteristics. However, battery characteristics such as power, energy, life and safety can vary among Li-ion battery designs [3]. The main factor governing this is battery chemistry, which is characterized by the materials used in cathode and anode. The most common anode material is graphite, however there are various cathode materials used in automobile applications [3,12]. Therefore, the Li-ion chemistry is often specified by the cathode material (assuming that the anode is graphite). Design parameters at the cell level (shape, electrode thickness, electrolyte material, etc.) and pack level (distance between the cells, connection elements, etc.) also affect performance and life.

Apart from the specific type and design of the battery, the conditions and stress factors during storage and use also affect how quickly the battery will degrade. There are various factors that affect battery life such as time, charge/discharge rate, temperature, and depth of discharge (DOD)/state of charge (SOC). The degree to which each of these factors affects degradation patterns depends on the chemistry and design. One type of cathode chemistry that has been extensively tested in the public literature is $LiFePO_4$ (LFP). LFP is promising due to its safety and longer life characteristics [13–15], although it has lower energy density than some alternative Li-ion chemistries.

Table 1 provides a list of reviewed studies that perform accelerated tests at different temperature, discharge/charge current rates (C-rate) and depths-of-discharge (DoD) to quantify degradation and to identify the effects of these factors on degradation. Most of these studies also provide insight on the underlying degradation mechanisms and conclude that the main mechanism of degradation for LFP is usable lithium loss due to SEI growth. Although SEI growth occurs during both storage and cycling, there is more capacity fade during cycling due to fresh SEI formation in the cracks that occur on the SEI layer with volume expansion and contraction during cycling [16,17]. The SEI growth usually increases with temperature and C-rate, however the magnitude varies in different studies. In addition, asymmetric cycles with different C-rates during charge and discharge can lead to different degradation behavior [18]. While Peterson et al. shows that LFP degradation is independent from DoD [19], Wang et al. and Groot et al. [18,20] report cycling at high DoD might create significant changes in degradation at high C-rates. Liu et al. argues that there is not a significant impedance growth in this chemistry [21]. On the other hand Groot et al. reports up to 30% impedance growth when the cycle C-rates are different during charge and discharge [18]. However, capacity fade is faster than impedance growth in these studies, relative to common EOL criteria. To sum up, various studies performed on LFP batteries show differences in the results they report, and there is, at present, no single model that can describe the degradation comprehensively.

In contrast, storage fade is primarily dependent on the temperature and the state-of-charge (SOC) at which the cells are stored.

Table 2
Thermal Management Systems Classification [31].

Purpose	• Heating • Heating and Cooling
Cooling medium	• Air • Liquid
Source	• Active (cooling medium pre-conditioned before entering the battery) • Passive

Several studies report that cells stored at higher SOC degrade at a faster rate [22,23]. The difference between capacity fade at two SOC levels decreases as the SOC levels increase [16,24].

Among the operational factors that affect LFP degradation, temperature is one of the most significant, because degradation increases exponentially with rise in the temperature [20,29,30]. Battery temperature is therefore often controlled in order to improve battery life. This control can be achieved by the various thermal management systems that are classified in Table 2. Currently, different vehicles in the market apply different cooling strategies (e.g.: the Toyota Prius PHEV uses air cooling; the Chevy Volt has a complex active liquid cooling system; the Nissan Leaf lacks a thermal management system; and the Tesla Model S, an electric vehicle with almost three times the energy capacity of the Nissan Leaf, has an active liquid cooling system.

There are many studies in the literature that examine and model cell/pack level thermal behavior [32–36] and thermal management design and control for battery packs [37–45]. However, studies that examine the battery life implications of thermal management are rare. In addition, the effects of various stress factors on cell level degradation are explored considerably, however there are only a few studies that investigate the implications of these factors in real world vehicle use conditions. Table 3 summarizes the studies that characterize the regional implications of one or more stress factors on battery life. Gross and Clark investigate the effect of thermal management on battery life using a generic battery life model, whose parameters they estimate based on the assumption that the capacity fade of the battery at the end of 15 years will be 20% when stored at 30 °C [46]. They then scale these parameters for other temperatures, by assuming that each 10 °C increase in temperature will double the fade rate. Smith et al. uses a comprehensive battery life model based on nickel-cobalt-aluminum (NCA) chemistry, however they do not specify a thermal management strategy in their analysis [47]. The most comprehensive analysis thus far was performed by Neubauer and Wood [48], in which they used the same battery life model as Smith et al., and compared the effect of different liquid cooling thermal management strategies on battery life.

In this study, we aim to assess the regional and drive cycle implications of degradation of a PHEV battery. For this purpose we construct a comprehensive and modular simulation model to address three main questions: 1) How much improvement in PHEV battery life can be obtained with passive air-cooling? 2) How does this improvement vary across different regions and different driving and usage profiles? 3) What is the sensitivity of the results to the model parameters and assumptions? Various case scenarios are simulated for an air-cooled PHEV battery pack with $LiFePO_4$/graphite chemistry cells.

In the following sections the approach of the study is described; details of each module are given with underlying assumptions; the simulations performed are explained; and finally the results, limitations and future work are discussed.

2. Approach

To address the questions listed above, we begin by creating usage scenarios for one year of daily driving, charging and rest conditions and record the battery usage history. We use the battery usage history to estimate the degradation over consecutive years, assuming that every year the same usage profile repeats itself.

We consider a vehicle with specifications similar to a Toyota Prius with a Hymotion ANR26650 $LiFePO_4$/Graphite pack composed of cylindrical cells manufactured by A123 systems [25]. This choice enables us to draw on prior work and use an air-cooled system with well-established parameters, and it illustrates the approach for use in future studies that may examine other vehicle and battery designs. Based on these assumptions, we develop a comprehensive simulation model to estimate battery temperature, current and state of charge profiles under the usage scenarios mentioned above. The model consists of three main simulation blocks: driving, charging and rest. In addition to these blocks, there are four sub-models, which can be used by one or more of the simulation blocks to perform necessary calculations. These sub-models are: battery equivalent circuit model (ECM), performance model, thermal model, and battery life model. For the purposes of the simulations in this study, we also create a decision algorithm that decides which simulation block to execute based on the travel patterns. The interactions between model components as well as the primary simulation inputs are given in Fig. 1, and each model component is explained in detail in the following sections.

Table 3
Studies that characterize the regional implications of battery life.

	Regional comparison	Thermal Management	Life model	Battery chemistry	Powertrain	Drive cycle comparison
Gross and Clark, 2011	Yes	Air vs Liquid	Function of temperature and time. Parameters estimated assuming 20% capacity fade at 30 °C, in 15 years, fade rate is doubled with each 10 °C increase	Not known	PHEV BEV	Yes
Smith et al., 2012 [47]	Yes	N/A	Function of temperature, time, number of cycles and depth of discharge. Parameters based on literature and experimental data	NCA	PHEV	Yes
Neubauer and Wood, 2014 [48]	Yes	No cooling vs liquid cooling, with three different control strategies	Function of temperature, time, number of cycles and depth of discharge. Parameters based literature and experimental data	NCA	BEV	Yes
This study	Yes	No cooling vs air cooling	Function of temperature, Ah-throughput, C-rate and time. Parameters based on literature	LFP	PHEV	Yes

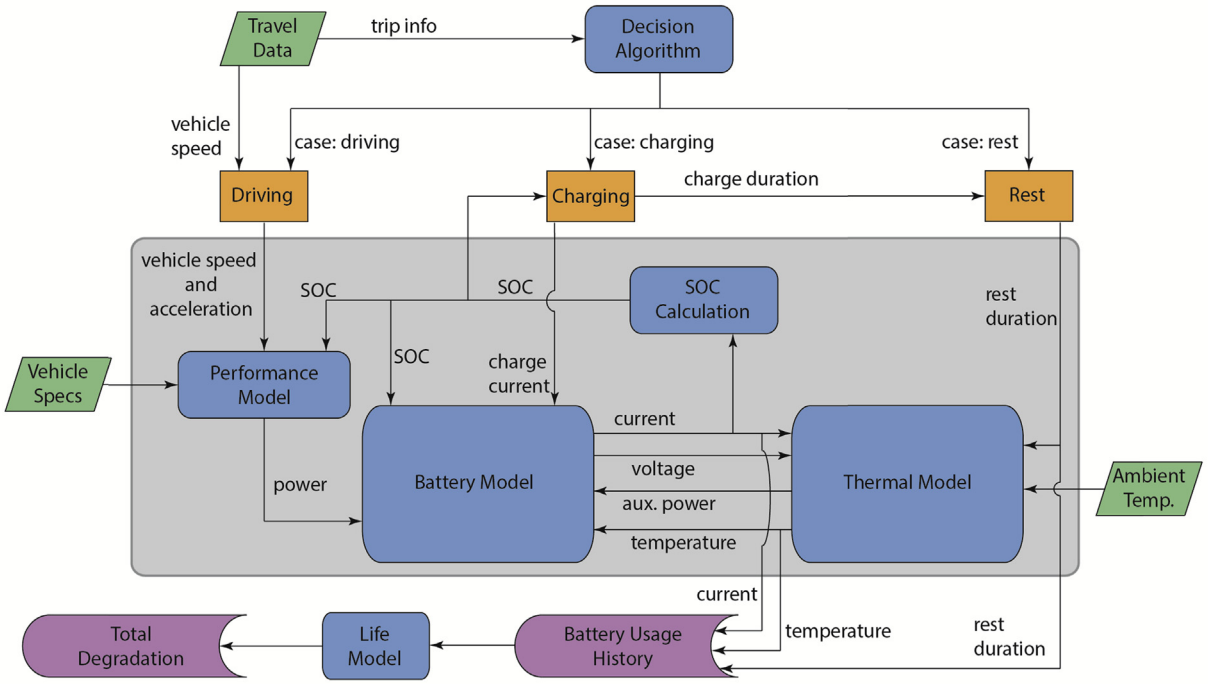

Fig. 1. Schematic of the modeling and simulation approach followed in the study.

2.1. Travel data

To estimate daily travel behavior of the vehicle, we use GPS sample data from the Atlanta Regional Commission (ARC) Regional Travel Survey with GPS Sub-Sample, available at the Transportation Secure Data Center (TSDC) of the National Renewable Energy Laboratory (NREL) [49]. The GPS sub-sample contains data for 1653 vehicles. We filtered the data for the vehicle types and models that might be comparable to plug-in hybrid vehicles available in the market. We selected four vehicle types; Auto Sedan, Auto 2-Seat, SUVs and Station Wagons, whose models are newer than the year 2000, which decreased the total number of vehicles to 921. Each of these vehicles has 3–7 days of travel data information available, and the total number of travel days in this subset of data is $N^{GPS} = 4940$. Here, it is assumed that each travel day in this dataset represents a different day of a single vehicle. For each GPS travel day k, the travel profile (φ_k^{GPS}) contains information on the number of trips the vehicle made each day (T_k^{GPS}), the onset $(t_{k\tau}^{START})$ and end times $(t_{k\tau}^{START})$ of each trip τ on each travel day k, and speed versus time points for each trip $v_{k\tau t}^{GPS}$ as summarized in Equation (1).

$$\varphi_k^{GPS} = \left\{ v_{k\tau t}^{GPS},\ t_{k\tau}^{START}, t_{k\tau}^{END} \right\}, \quad \begin{array}{c} t = 0, 1, .., t_{k\tau}^{LENGTH} \\ t_{k\tau}^{LENGTH} = \left(t_{k\tau}^{END} - t_{k\tau}^{START} \right) \\ k = 1, 2, \ldots, N^{GPS} \\ \tau = 1, 2, \ldots, T_k^{GPS} \end{array} \tag{1}$$

To create a one year long hypothetical usage scenario, we first assume there are no trips for 121 days of the year during which the vehicle will be at rest [50]. For the rest of the year, we pick $N^{YEAR} = 244$ travel days from $N^{GPS} = 4950$ available in the GPS data to represent 1 year of driving conditions. We draw travel days randomly until we find a set of 244 travel days that total between 11,000 and 15,000 miles, in order to seek data representative of U.S. driving [51].

To test the sensitivity of the results to drive cycle, we also perform simulations using two standard fuel economy test cycles used by the Environmental Protection Agency (EPA). The first cycle, the Urban Dynamometer Driving Schedule (UDDS), represents city driving conditions [52]. The second cycle we use is US06, an aggressive (high acceleration) driving schedule [52]. To incorporate test cycles into the simulations, we employ two different approaches, which we describe in Section 2.7.

2.2. Decision algorithm

The decision algorithm decides which block (driving, charging or rest) to execute in which order based on the travel pattern each day. If the day is a rest day, the 'rest' block is simulated. If it is a travel day, each block is called in an order that is determined by onset times of the trips and duration between trips. Charging begins immediately following the last trip of the day. The vehicle is assumed to be at rest in between trips and after charging until the next day's trip.

2.3. Simulation procedure

In this section, a sample day of simulations with a single trip is used to explain the simulation procedure. For this simulation day, it is assumed that the driving, charging and rest blocks are simulated one after another.

The *Driving block* takes trip speed profile $v(t)$ as an input and uses performance, battery and thermal models to estimate the dynamic current and temperature profile during the trip. Charging starts immediately after the last trip of the day. The *Charging block* first decides the duration of the charging based on the remaining capacity in the battery after driving. During this duration, it uses battery and thermal models to estimate the battery temperature. Charge duration is calculated as:

$$t^{CHG} = \frac{(0.9)(C^{RATED}) - \left(\Phi_{t^{DRVEND}}^{SOC}\right)(C^{RATED})}{I^{CHG}} \tag{2}$$

where t^{CHG} is the charge duration, C^{RATED} is the battery rated

capacity, $\Phi^{SOC}_{t^{DRVEND}}$ is the SOC level at the end of driving, and I^{CHG} is the charging current. We assume the battery is charged up to 90% of its rated capacity, and full (100%) charging is avoided. We assume constant current charging at 4.6 A. This value is estimated based on the Hymotion battery pack specifications, in which it is mentioned that it takes 5.5 h to charge the 25.3 Ah battery [53]. Once charging is complete, the *rest block* determines the duration the vehicle will be at rest based on the charging duration and the start of the next day's trip. Rest duration is then used as an input to the thermal model to estimate battery temperature.

2.3.1. Performance model

The performance model calculates the power drawn from the battery to sustain a certain speed profile based on the vehicle specifications and is then used as an input to the battery model and thermal model to estimate the current and temperature profiles. The model estimates power assuming two modes of operation: charge depleting (CD) and charge sustaining (CS) modes. We assume the CD mode to be all-electric, with the battery being the only power source. The CD mode is maintained until the state-of-charge (SOC) reaches a minimum preset value, which we set to 20%. In other words, we assume the SOC swing to be between 90 and 20%. When the minimum SOC level is reached, the vehicle operation switches to CS mode. In CS mode, the battery SOC is kept at the target level. This procedure can be summarized as follows:

$$P_t = \left\{ \begin{array}{ll} P_t^{CD}\left(v_t, a_t, \psi^{VEH}\right), & if\ t \le t^{CDEND} \\ P_t^{CS}\left(v_t, a_t, \psi^{VEH}\right), & else \end{array} \right\}$$
$$\psi^{VEH} = \left[m^{VEH}, C^{DRAG}, A^{FRONT}, C^{RR}, \eta^{RB}, \eta^{BW}\right] \quad (3)$$
$$\text{where } t^{CDEND} = \min\left\{t : \Phi_t^{SOC} \le \Phi^{SOC,MIN}\right\}$$

where P_t is the power drawn from the battery at time step t, which is either equal to the power at CD mode (P_t^{CD}) or CS mode (P_t^{CS}). v_t and a_t are the vehicle speed and acceleration during the trip, Φ_t^{SOC} is the state-of-charge at time step t, and t^{CDEND} is the time step when $\Phi_t^{SOC} \le \Phi^{SOC,MIN}$ for the first time ($\Phi^{SOC,MIN} = 0.2$). ψ^{VEH} is a vector of constant parameters: vehicle mass (m^{VEH}), drag coefficient (C^{DRAG}), vehicle frontal area (A^{FRONT}), tire rolling resistance coefficient (C^{RR}), efficiency of power transfer from regenerative breaking to battery (η^{RB}) and efficiency of power transfer from battery to wheels (η^{RB}).

In CD mode, the power load on the battery is calculated using a similar approach presented in Peterson et al. [19]. The power P_t^{CD} drawn from the battery in CD mode can be calculated using Equation (4).[1]

$$P_t^{CD} = \left\{ \begin{array}{ll} \eta^{RB}\left(m^{VEH}a_t + \frac{1}{2}\rho^{AIR}v_t^2 C^{DRAG}A^{FRONT} + C^{RR}m^{VEH}g\right)v_t, & regen \\ \dfrac{\left(m^{VEH}a_t + \frac{1}{2}\rho^{AIR}v_t^2 C^{DRAG}A^{FRONT} + C^{RR}m^{VEH}g\right)v_t}{\eta^{BW}}, & otherwise \end{array} \right. \quad (4)$$

[1] In the original Hymotion system the Li-ion battery pack does not receive any regenerative charging, however the NiMH battery does. Here, since we assume the full pack is the Li-ion design, we assume regenerative charging is accepted by this pack.

where g is the gravitational acceleration, and ρ^{AIR} is the air density. In the equation "regen" corresponds to regenerative braking that occurs when $a_t<0$.

In CS mode, in order to obtain the battery current and voltage profile, it is necessary to model the power control strategy. We adopt the dynamic model of the Toyota hybrid powertrain system developed by Liu and Peng for this purpose [54]. The MATLAB/Simulink® based model was developed to test powertrain control strategies. It takes the vehicle specifications and the drive cycle as inputs and evaluates the vehicle performance using mathematical models of the engine, generator, electric motor, controller, and battery. We modify the Liu and Peng model by replacing its battery model with the equivalent circuit model described in Section 2.3.2. We also incorporate a thermal model (Section 2.5). The remainder of the Simulink model is treated as a black-box function that determines power load on the battery in CS mode (P_t^{CS}). For more details on the Simulink model the interested reader is referred to [54,55].

2.3.2. Battery model

The battery model estimates the current and voltage profile of the battery under a power load. The battery pack consists of 14 modules connected in series. Each module has 44 cells, and the cells are connected with a configuration of 11 parallel - 4 series [56]. Pack current and voltage profiles can be estimated by evaluating each cell's electrical performance. The current drawn from each cell of the pack at each time step t is:

$$I_t = \left\{ \begin{array}{ll} \dfrac{\left(P_t + P_t^{AUX}\right)/N^{CELL,PACK}}{V_t}, & driving \\ I^{CHG}/N^{CELL,PARALLEL}, & charging \end{array} \right. \quad (5)$$

where P_t is the total power drawn from the pack at time t, I_t is the current drawn from each cell (which is negative during regeneration braking and charging), $N^{CELL,\ PACK}$ is the total number of cells in the battery pack, $N^{CELL,\ PARALLEL}$ is the number of the cells connected in parallel and V_t is the cell voltage. P_t^{AUX} is the power consumed by the auxiliary equipment. The main auxiliary power we consider in this study is the HVAC power consumption, which is explained in more detail in Section 2.5.

The electrical behavior of the cells can be modeled using an equivalent circuit model (ECM). The generic equations for the circuit model used in this study can be defined as follows:

$$V = V^{OCV} - I\cdot R^{OHM} - V^{D1} - V^{D2} \quad (6)$$

$$\dot{V}^{D1} = -\frac{1}{R^{D1}C^{D1}}V^{D1} + \frac{1}{C^{D1}}I \quad (7)$$

$$\dot{V}^{D2} = -\frac{1}{R^{D2}C^{D2}}V^{D2} + \frac{1}{C^{D2}}I \tag{8}$$

In this model, V^{OCV} is the open circuit voltage of the battery, R^{OHM} is the Ohmic resistance, and V is the battery voltage. The voltage-drops V^{D1} and V^{D2} across the resistance-capacitor (RC) couples represent the dynamic voltage losses. The current I is assumed to be positive during discharge. Equations (7) and (8) are ordinary differential equations, which can be discretized for each time step.

$$V_{t+1}^{D1} = V_t^{D1} e^{-\frac{1}{R_t^{D1}C_t^{D1}}t^S} + R_t^{D1} I_t \left(1 - e^{-\frac{1}{R_t^{D1}C_t^{D1}}t^S}\right) \tag{9}$$

where t^S is the sampling period (i.e. the time difference between two time steps; $t^S = 1$ s in our analysis). Then the battery voltage at each time step can be solved as:

$$V_t = V_t^{OCV} - I_t \cdot R_t^{OHM} - V_t^{D1} - V_t^{D2} \tag{10}$$

The ECM parameters are functions of SOC and battery temperature. Perez et al. estimated the model parameters for A123 Systems 26650 LFP/graphite cells [57] and they provide the parameters as look-up tables for each parameter, consisting of their values at 8 different temperature and 9 different SOC index points in Ref. [58]. We estimate the parameters at each time step by linear interpolation between the values provided in each look-up table. For example, the Ohmic resistance at each time step is:

$$R_t^{OHM}\left(\Phi_t^{SOC},\ T_t^{CELL}, \mathbf{\Phi}^{SOCINDEX}, \mathbf{T}^{INDEX}\right) \tag{11}$$

where, Φ_t^{SOC} is the state of charge and T_t^{CELL} is the cell temperature at each time step t, and $\mathbf{\Phi}^{SOCINDEX}$ and $\mathbf{T}^{INDEX}$ are the SOC and temperature indices of the look-up table.

Although some studies showed that the open circuit voltage (V^{OCV}) depends on the temperature [59], many studies in the literature neglect the temperature dependence of the open circuit voltage. In addition, Lam et al. [60] showed that the deviation of V^{OCV} at different temperatures from its reference value at 25 °C is less than 2 mV at most temperatures. Therefore, it is a reasonable approximation to assume that V^{OCV} will not change with temperature and that it depends only on SOC. Herein, we use the SOC dependent V^{OCV} data from Perez et al. [57] for the simulations:

$$V_t^{OCV}\left(\Phi_t^{SOC}\right) \tag{12}$$

2.4. State-of-charge estimation

The state-of-charge (SOC) at each time step needs to be estimated for the interpolation of ECM parameters as well as to decide in which operation mode the vehicle is operating (CD or CS). In this study, we approximate Φ_t^{SOC} as follows:

$$\Phi_{t+1}^{SOC} = \frac{\Phi_t^{SOC} C^{RATED} - I_t\left(\frac{t^S}{3600}\right)}{C^{RATED}} \tag{13}$$

where C^{RATED} is the cell rated capacity in ampere-hours (Ah) and t^S is the time difference between two steps in seconds. Note that we define the SOC based on the rated capacity (which is constant) rather than available capacity (which decreases over time). Our approximation based on rated capacity is valid until 30% capacity loss, since we assume that SOC of the battery swings between 90% and 20%, i.e. only 70% of the capacity is used. To see the effect of this assumption on degradation, we ran a sensitivity case where SOC is based on available capacity and we found there can be up to 4% less degradation in this case. The results from this case study are provided in the supplemental information.

2.5. Thermal model

The thermal model approximates the battery temperature at each time step by[2]:

$$T_{t+1}^{BAT} = T_t^{BAT} + \frac{\dot{Q}_t^{GEN,BAT} - \dot{Q}_t^{TR}}{M^{BAT}}\, t^S \tag{14}$$

where T_t^{BAT} is the battery temperature, $\dot{Q}_t^{GEN,BAT}$ is the heat generation rate inside the battery, $\dot{Q}_t^{TR}$ is the heat transferred to or from the battery, and M^{BAT} is the battery thermal mass.

In constructing this thermal model, a series of assumptions were made. First, the temperature difference across the cell is neglected. The temperature of a cylindrical cell under dynamic conditions may vary radially (core and surface temperature difference) due to different layers of materials the cell spiral consists of, as well as in longitudinal direction due to the location of tabs and connectors. What determines the cell degradation and performance is peak temperatures typically is the hottest part of the cell – typically the cell core temperature rather than the surface temperature. There are many studies in the literature that aim to model this thermal behavior of the cell [61–63], however, none of these studies provide validation since it is not always easy to measure the core temperature of the battery. Most of these studies show by modeling and simulation that the difference between the cell core and surface temperatures is negligible under low C-rates and may increase up to 5 °C at higher C-rates. Ye et al. [64], on the other hand, shows that the temperature difference for a cylindrical LFP cell - with similar parameters to the cell used in this study - can reach up to 10 °C under strong forced convection conditions, which might alter the final degradation profiles for the batteries. However, the possible temperature difference across the cell is assumed to be negligible in this study, and further investigation of this issue is left for future work. We also assume that the temperature is uniform across the battery pack, i.e. there is no cell-to-cell temperature variance. We neglect any conduction between the cells as well as between cells and outer materials. Given the cell degradation rate's non-linear dependence on temperature, the assumption of uniform temperatures is likely to yield optimistic estimates of battery life. Zheng et al. [65] and Chiu et al. [66] show that the temperature difference across cells connected in series can cause the pack degradation to be 2–6% larger compared to the average cell degradation. A high-resolution approach for quantifying this effect would require a more complex thermal model of both the battery and the thermal management system, and would not be practical for the type of simulations in this study. Instead, to estimate the effect of cell-to-cell temperature variation on degradation, we consider two new scenarios: (1) Optimistic: Each module in the pack is divided into three sub-modules, where the outlet air from one sub-module is the inlet to the next. With this approach, we aim to capture temperature variation caused by air warming while passing through the module, which creates a lower bound on cell-to-cell variation. (2) Pessimistic: We assume one cell in the pack

[2] Heat removed from the battery is considered positive (+) and heat transfer into the battery is negative (−).

constantly runs 5 °C hotter than the rest of the pack during operation – a conservative approach to create an upper-bound. With the first approach, there is no change in the degradation profile, whereas in the second approach we observe a 3% increase in degradation. We report and discuss the results in the supplementary information.

The heat generated in the battery pack is equal to the sum of the heat generation in each cell. Heat generation in the pack can be approximated as:

$$\dot{Q}_t^{\mathrm{GEN,BAT}} = N^{\mathrm{CELL,PACK}} I_t \left(V_t^{\mathrm{OCV}} - V_t\right) \tag{15}$$

With the formulation above, we have assumed that all cells exist in an identical state and generate identical amounts of heat. Non-uniform cell degradation will cause greater heat generation in more degraded cells placed in series. Note that in this approximation we neglect reversible heat generation.

The heat transfer mechanisms we consider are the convection and conduction from the battery pack to cabin and ambient as well as forced convection heat transfer with air cooling:

$$\dot{Q}_t^{\mathrm{TR}} = \begin{cases} \dot{Q}_t^{\mathrm{TR,FC}} + \dot{Q}_t^{\mathrm{TR,NC}}, & v^{\mathrm{AIR}} \neq 0 \\ \dot{Q}_t^{\mathrm{TR,NC}}, & v_t^{\mathrm{AIR}} = 0 \end{cases} \tag{16}$$

where $\dot{Q}_t^{\mathrm{TR}}$ is the total heat transfer from the battery, $\dot{Q}_t^{\mathrm{TR,FC}}$ is the heat transfer by forced air convection, v_t^{AIR} is the speed of the air entering the battery during cooling and $\dot{Q}_t^{\mathrm{TR,NC}}$ is the heat transferred from the battery to the cabin and outside by natural convection and conduction. To estimate $\dot{Q}_t^{\mathrm{TR,FC}}$, we construct an air cooling model of the battery pack. We evaluate $\dot{Q}_t^{\mathrm{TR,NC}}$ using the thermal network model developed in NREL [48,67]. The details of these models are explained in the next sections.

2.5.1. Air cooling model

The battery pack is cooled by a fan that draws cabin air to the battery. We assume a simple on-off thermal control strategy, in which the fan is turned on and off when the battery temperature reaches and falls down to pre-determined threshold values, as given in Equation (17). When the fan is on, the air speed is fixed at 17 m^3/h (cubic meter per hour), which is the lowest battery fan speed for Toyota Prius Hybrid battery [68]:

$$v_t^{\mathrm{AIR}} = \begin{cases} 17\ \left[m^3/h\right], & T_t^{\mathrm{BAT}} > 35^o C \\ 0, & otherwise \end{cases} \tag{17}$$

The flow of air is divided in parallel so that same amount of air passes through each module in the pack [56]. Therefore, we only model and simulate one single module to obtain the representative temperature of the whole pack under air-cooling. A picture of the battery pack, as well as an illustration of the cell configuration inside a module is given in Fig. 2.

The heat transfer with forced air convection from cells inside the module can be estimated by:

$$\dot{Q}_t^{\mathrm{TR,FC}} = N^{\mathrm{CELL,MODULE}} h \pi D^{\mathrm{CELL}} \Delta T_t^{\mathrm{LM}} L^{\mathrm{CELL}} \tag{18}$$

In this equation, h is the overall heat transfer coefficient, D^{CELL} is the cell diameter, ΔT_t^{LM} is the log mean temperature difference at each time step and L^{CELL} is the cell length. The overall heat transfer coefficient h is defined as:

$$h = Nu_D \cdot k^{\mathrm{AIR}} / D^{\mathrm{CELL}} \tag{19}$$

where Nu_D is the Nusselt number, and k^{AIR} is thermal conductivity of air. The cell configuration inside the pack is neither fully aligned nor fully staggered. However, it has mostly a staggered arrangement and therefore in this study the correlation in Equation (20) by Zhukauskas [70] for "flow across staggered bank of tubes" at uniform surface temperature is used to estimate the Nusselt number.

$$Nu_D = C\left(Re_{D,max}\right)^m (Pr)^{0.36} \left(Pr/Pr_s\right)^{0.25} \tag{20}$$

$Re_{D,max}$ is the Reynolds number calculated at maximum air velocity, C and m are constants obtained empirically and tabulated for $Re_{D,max}$, and Pr is the Prandtl number. $Re_{D,max}$ and Pr are calculated at the film temperature, T^{FILM}, which is defined as:

$$T^{\mathrm{FILM}} \equiv \left(T^{\mathrm{SURF}} + T^{\mathrm{AIR}}\right)/2 \tag{21}$$

where T^{SURF} is the cell surface temperature and T^{AIR} is inlet air temperature. Pr_S is calculated at T^{SURF}.

In this study, we assume that air inlet temperature T^{AIR} is equal to the cabin temperature, which is kept constant at 24 °C. In addition, we assume that cell temperature is uniform radially and axially along each cylindrical cell. Therefore, cell surface temperature is actually the cell temperature overall, i.e. $T^{\mathrm{SURF}} = T^{\mathrm{CELL}}$. Since cell temperature is time dependent, ($T^{CELL}(t)$), Pr and Pr_S should also vary at each time step. However, change of air Prandtl number with temperature is considerably small, therefore we assume a constant Prandtl number $Pr = Pr_S = 0.71$. Therefore, a constant heat transfer coefficient h is calculated for forced air-cooling.

The log mean temperature ΔT_t^{LM} difference in Equation (18) is

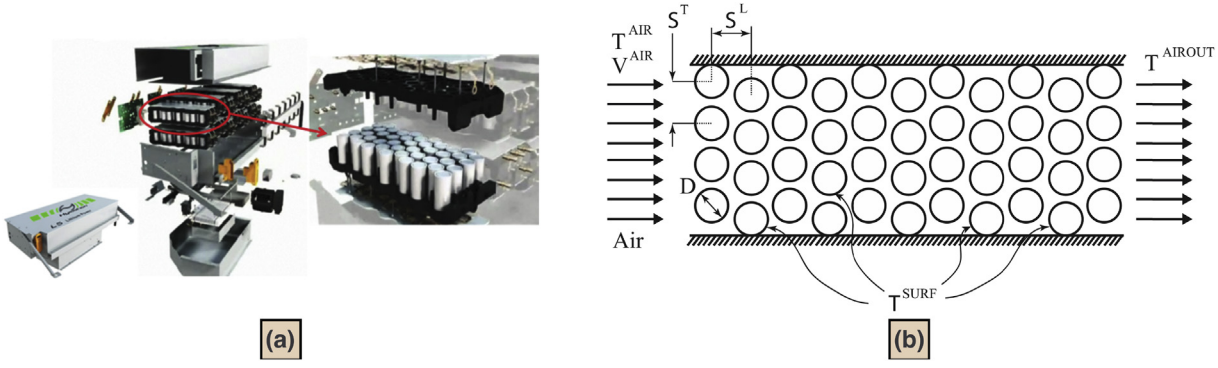

Fig. 2. **(a)** A123 Systems Hymotion Li-ion conversion battery pack (Image Source: A123 Hymotion Animation [69]) **(b)** An illustration of the cell configuration inside a single module.

defined as:

$$\Delta T_t^{LM} = \frac{\left(T_t^{SURF} - T^{AIR}\right) - \left(T_t^{SURF} - T_t^{AIROUT}\right)}{\ln\left(\frac{T_t^{SURF} - T^{AIR}}{T_t^{SURF} - T_t^{AIROUT}}\right)} \quad (22)$$

where T_t^{AIROUT} is the temperature of air leaving the battery, and it can be calculated by using the relation given in Equation (23), which can be obtained by equating the heat transferred from the cell surfaces to air (Equation (18)) to the heat carried away by air.

$$\left(\frac{T_t^{SURF} - T_t^{AIROUT}}{T_t^{SURF} - T^{AIR}}\right) = exp\left(-\frac{\pi D^{CELL} N^{CELL,MODULE} h}{\rho^{AIR} v_t^{AIR} A^T c^{AIR}}\right) \quad (23)$$

where ρ^{AIR} is air density, v_t^{AIR} is the air speed, A^T is the air inlet area, and c^{AIR} is the air constant specific heat.

2.5.2. Thermal network model

We estimate the heat transfer from the battery to the ambient and to the cabin using the thermal network model developed in Refs. [48,67]. According to this model the heat transferred from the battery is estimated as:

$$\dot{Q}_t^{TR,NC} = K^{ab}\left(T_t^{BAT} - T_t^{AMB}\right) + K^{bc}\left(T_t^{BAT} - T_t^{CAB}\right) \quad (24)$$

where T_t^{AMB}, T_t^{CAB} and T_t^{BAT} are ambient, cabin and battery temperature. K^{ac} is the thermal resistance between cabin and ambient, K^{ab} is the thermal resistance between battery and ambient, and K^{cb} relates the battery conduction to cabin. Thermal resistances were estimated by fitting values to the data collected in December 2008 in Golden, CO with a Gen 2 Toyota Prius. Cabin temperature can be estimated as:

$$T_{t+1}^{CAB} = T_t^{CAB} - \frac{\dot{Q}_t^{CAB}}{M^{CAB}} \quad (25)$$

where M^{CAB} is the vehicle cabin thermal mass, and $\dot{Q}_t^{CAB}$ is the heat transfer rate from the cabin defined by:

Table 4
Values of coefficient ***A*** in equation (29) as given in Wang et al. [20].

$C^{RATE}=I^{CELL}/C^{CELL}$	1/2	2	6	10
A	31,630	21,681	12,934	15,512

$$\dot{Q}_t^{CAB} = \frac{T_t^{CAB} - T_t^{AMB}}{K^{ac}} + \frac{T_t^{CAB} - T_t^{BAT}}{K^{bc}} - \dot{Q}_t^{RAD} + \dot{Q}_t^{HVAC} \quad (26)$$

where $\dot{Q}_t^{RAD}$ is the radiative heat transfer and $\dot{Q}_t^{HVAC}$ is the heat removal from the cabin by HVAC system. We estimate the radiative heat transfer as:

$$\dot{Q}_t^{RAD} = \dot{q}_t^{SOLAR} \varepsilon A^{CAR} \quad (27)$$

$\dot{q}_t^{SOLAR}$ is the global diffuse horizontal radiation per unit area that can be found in "Typical Meteorological Year" database compiled by NREL for various cities in United States [71]. ε is the surface emissivity and A^{CAR} is the car surface area. In the model, $\dot{Q}_t^{HVAC}$ is estimated as:

$$\dot{Q}_t^{HVAC} = \begin{cases} 4500\ W, & T_t^{CAB} > 25^oC \\ -4000\ W, & T_t^{CAB} < 19^oC \\ 0, & otherwise \end{cases} \quad (28)$$

The detailed schematic descriptions with the input-output relationships for each model are provided in the Supplemental Information.

2.6. Battery degradation model

Li-ion batteries degrade with time and usage. Degradation occurs due to various reactions and processes both in electrolyte and electrode level, and these can show differences between different chemistries.

We focus on the $LiFePO_4$ (LFP) chemistry. The main reasons for this choice are: (1) the cells used in the actual Hymotion battery pack are of this chemistry, (2) due to its safety and longer life characteristic, this chemistry is a potential candidate to be used in automotive applications, and it has been extensively studied in the

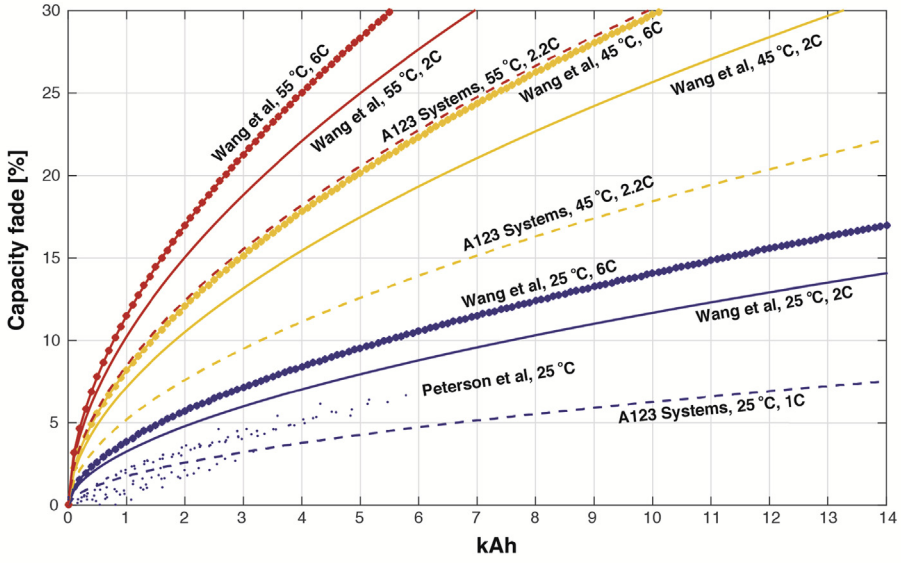

Fig. 3. Percent capacity fade with Ah-processed during cycling of A123 Systems ANR26650 cell - comparison of results from different studies.

Table 5
Case studies simulated.

Test the effect of:	Options
Thermal management	No battery thermal management Air-cooling
Regional Climate	San Francisco, CA Phoenix, AZ Miami, FL
Driving Cycle	GPS data from Atlanta EPA US06 test cycle EPA UDDS test cycle
Annual miles driven	12,400 miles 14,700 miles

public literature [14,19–21,26–28], and (3) in this chemistry, the main aging is due to capacity loss rather than impedance growth [19,21], therefore the battery life model can be simplified by considering only capacity loss criteria. In LFP batteries, the main aging mechanism is SEI growth, therefore the degradation modeling approach we follow here is similar to other batteries where SEI growth is the dominant factor in ageing.

Fig. 3 shows the percent capacity fade versus Ah-processed obtained from the studies in Table 1 that tested A123 Systems ANR26650 cells. As can be seen from the figure, measurements and/or estimations of degradation vary a lot among studies and test conditions. We select the model provided by Wang et al. as our base case model, since it provides the most comprehensive analysis considering the main stress factors.

The generic capacity fade model described in Wang et al. is given in Equation (29):

$$\theta^{CYC} = A \cdot exp\left[\frac{-31700 + 370.3 \times \left(I^{CELL}/C^{CELL}\right)}{R^{GAS} \cdot T^{CELL}}\right]\left(\phi^{AH,TH}\right)^{0.55} \quad (29)$$

where θ^{CYC} is the percent capacity fade with cycling, I^{CELL} is the current drawn from (or charged to) the cell, C^{CELL} is the nominal cell capacity in ampere-hours (Ah), R^{GAS} is the universal gas constant, T^{CELL} is the cell temperature and $\phi^{AH,TH}$ is the ampere-hour (Ah) throughput. A is a constant given at four different C-rates (I^{CELL}/C^{CELL}) in Table 4. Note that in this equation, the relationship between degradation and temperature is formulated with an Arrhenius type relation.

The Ah-throughput in this model is defined as the energy delivered by the cell during cycling. Therefore, it does not involve the energy recharged to the cell during charging. We assume that the degradation mechanisms during the charging follow the same pattern as discharge, and we define a new parameter, Ah-processed ($\phi^{AH,PR}$) as the total energy processed in a cell (charge and discharge). Therefore, replacing $\phi^{AH,TH}$ with $\phi^{AH,PR}/2$ in Equation (29), we update the model as:

$$\theta^{CYC} = A \cdot exp\left[\frac{-31700 + 370.3 \times \left(I^{CELL}/C^{CELL}\right)}{R^{GAS} \cdot T^{CELL}}\right]\left(\phi^{AH,PR}/2\right)^{0.55} \quad (30)$$

We assume this generic model can be applied to estimate the cycling fade at each time step as follows:

$$\theta_t^{CYC} = \Gamma_t \cdot \left[\left(\frac{\theta_{t-1}^{CYC}}{\Gamma_t}\right)^{\frac{1}{0.55}} + \Delta\phi_t^{AH,PR}\right]^{0.55}$$
$$\Gamma_t = A_t \cdot (1/2)^{0.55} \cdot exp\left[\frac{-31700 + 370.3 \times C_t^{RATE}}{R^{GAS} \cdot T_t^{CELL}}\right] \quad (31)$$

where $\Delta\phi_t^{AH,PR}$ is the ampere-hour processed between the time steps t and $t-1$:

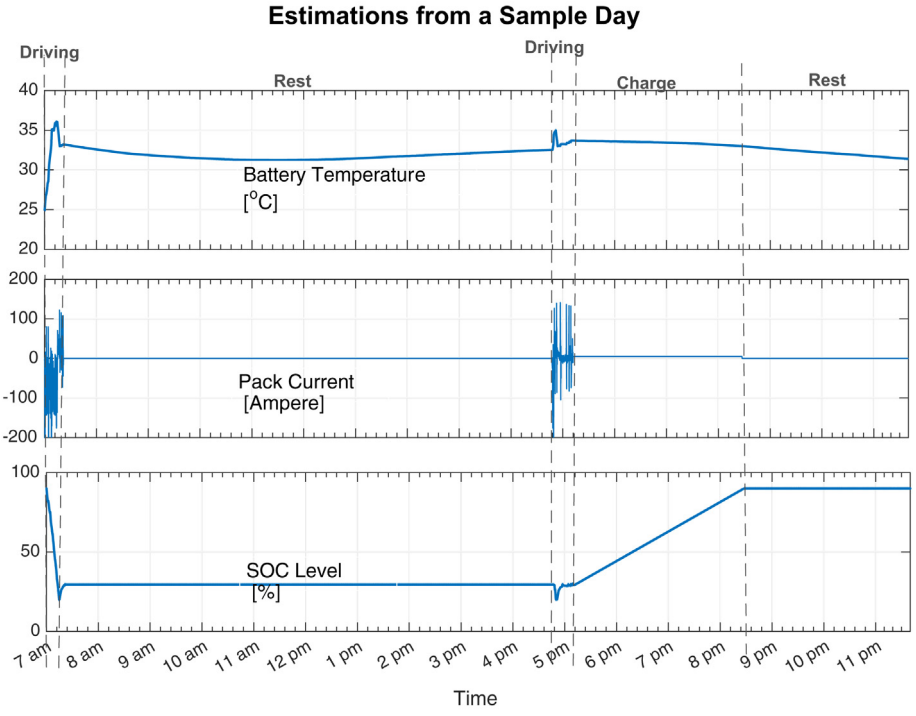

Fig. 4. Battery temperature, pack current and pack SOC level estimations from a 17 h duration of a sample day. The sample day is randomly selected from the case simulated in Phoenix with GPS data when air-cooling is employed during driving and charging to cool the pack when its temperature increases above 35 °C. The rest period prior to the 17-h period is excluded here to help make more detail visible during the short driving periods.

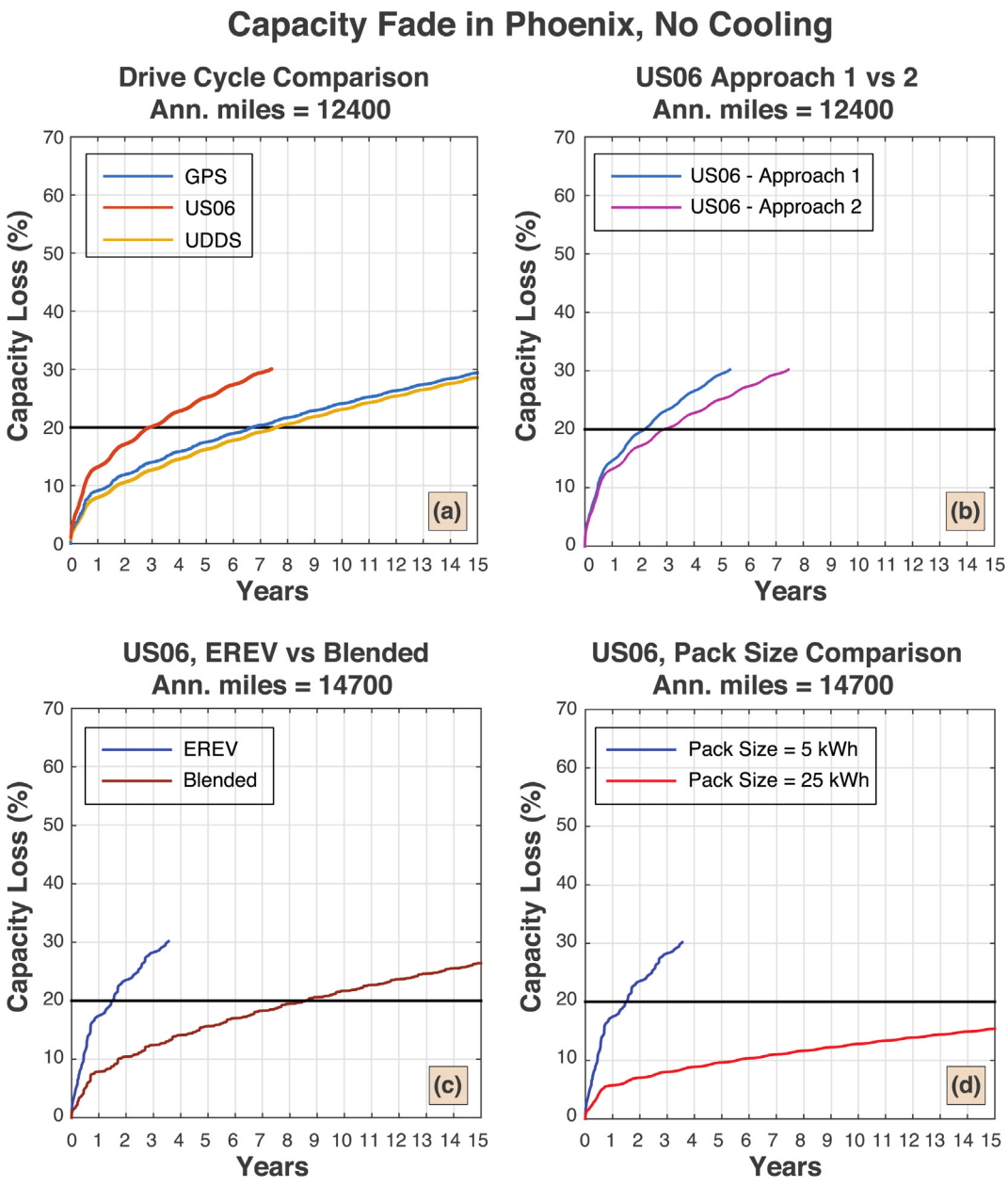

Fig. 5. Analyzing the drive cycle effect on capacity fade when air-cooling is not active. **(a)** Comparison of drive cycles in Phoenix. Annual miles driven are 12,400 miles. UDDS and US06 results are obtained using Approach 2: assuming same driving profile and distance every driving day **(b)** Comparison of two approaches in using US06 drive cycle. Approach 1: replace every trip in GPS data with corresponding US06 cycles that matches the same trip distance. Approach 2: assume same miles of travel every day divided into two trips, one in the morning and one in the evening **(c&d)** Investigation of capacity fade with US06. Annual miles driven are 14,700. (c) comparison of energy management strategies. (d) comparison of pack size.

$$\Delta\phi_t^{\mathrm{AH,PR}} = \int_{t-1}^{t} I^{\mathrm{CELL}}(t)\cdot dt \cong \frac{1}{2}\left(\left|I_t^{\mathrm{CELL}}\right| + \left|I_{t-1}^{\mathrm{CELL}}\right|\right) \tag{32}$$

We estimate A_t for C_t^{RATE} by using linear interpolation between the tabulated values given in Table 4.

The capacity loss during storage, i.e. whenever the vehicle is at rest, is obtained by a model fit to data provided by the cell manufacturer [22]. In the given data, the percent capacity loss was observed to vary linearly with the logarithm of time in days. Therefore, the model form given in Equation (33) is used to estimate the storage fade. The constant parameters given in the formula are obtained using least squares regression fit to the data.

$$\theta^{\mathrm{STO}} = \left(10^{0.0202\cdot T^{CELL}-5.885}\right)\cdot \log_{10}\left(t^{\mathrm{STO}}\right) \tag{33}$$

where t^{STO} is the storage duration in days.

Using this model for the purpose of estimating battery life in electrified vehicle applications requires several assumptions:

- The cycling tests were performed at static loading profiles, i.e. using constant current/discharge rates. We assume the same degradation model will be valid with under dynamic load, and that we can apply the model at 1-s resolution.
- The tests were performed on single cells only. We assume the degradation behavior does not change when the cells are used in connection with other cells in a pack.

- The coupled effects of stress factors are not clear. We assume the relationships observed in these tests are applicable when the model is used to estimate degradation at various other temperature and C-rate combinations.
- We assume the ageing mechanisms are exactly the same during charge and discharge. Li et al. shows that fresh SEI formation with cycling occurs only during charging and although this SEI peels off and accumulates during discharge, no new SEI formation occurs [16]. In addition, Groot et al. shows that different charge/discharge current combinations can lead to different capacity loss profiles depending on the temperature [18]. As an example, their test results indicate that for temperatures higher than 30 °C cycling with 1C discharge/3.75 C charge rates cause faster degradation than cycling with 3.75C both during charge and discharge.
- When estimating the constant parameter A_t in Equation (31) using Table 4, we assume for any C-rate lower or higher than the minimum and maximum index values given in the table, the constant A_t is equal to its value at either in the lowest or highest C-rate. Therefore, our estimates of degradation for C-rates higher than 10C are likely optimistic.

All these assumptions may be causing over or underestimation of degradation depending on the conditions. However, to Authors' knowledge, there is no model available in public literature that would address all these issues. We use sensitivity analysis to explore alternative assumptions and focus on comparing cases on a relative, rather than absolute, basis.

2.7. Simulations and sensitivity analysis

Using the procedure and models described above, we perform various simulations to estimate the effects of air-cooling, regional climate, and drive cycle on battery life. Table 5 summarizes the case studies simulated.

Thermal management: To test how much air-cooling improves battery life we simulate two cases. In the first case, there is no cooling system for the battery, and the interaction between battery, ambient and cabin is considered using only the thermal network model. In the second case, we assume battery is cooled with the forced convection air-cooling system described in Section 2.5.1.

Regional climate: We perform simulations for three different cities. Phoenix represents a region where cold hours as well as high peak temperatures can be observed. Both Miami and San Francisco show little hourly and daily fluctuations in temperature. However, in Miami the temperatures are higher, so Miami represents a hot climate, and San Francisco represents a mild climate in this study. The factors that change with region are the ambient temperature and radiation inputs to the thermal model.

Driving cycle: Changing drive cycle affects average vehicle speed so that it is not possible to compare two different drive cycles while holding both distance and time of trips constant. We compare results using two approaches:

Approach 1. In the first approach, the speed profiles in the GPS data are replaced by UDDS and US06 speed profiles repeated back-to-back such that the total distance driven remains the same. In doing this, we assume that the start time of each trip in the GPS data doesn't change. However, due to different speed profiles, trips can take longer or shorter with UDDS and US06, and therefore trips end times are different than the GPS data. This is a particular issue with UDDS, since it is a low speed cycle and the next trip start time in the GPS data may be earlier than the prior trip end time under UDDS driving. This results in instances of more than one trip occurring during the same hourly bin.

Approach 2. In the second approach we assume the same driving pattern every day throughout the year, with the same drive cycle (UDDS or US06). We divide the total annual miles driven to 244 driving days and assume half of this distance is driven in the morning starting at 8:30 a.m., and the other half is driven in the evening starting at 5:30 p.m., to represent a daily commute between home and work. We assume the battery is only charged after the last trip of the day and is at rest in between trips.

Annual miles driven: We pick two different sets of driving days drawn randomly from the GPS data. The first set sums up to a total distance of 12,400 miles and the second set has an annual mileage of 14,700 miles. Note that, we make these random selections based on distance only. Therefore, the two different sets also have other differences in driving patterns. However, the rest days and the driving days throughout the year are assumed to be the same across the two sets.

3. Results and discussion

3.1. Sample daily estimations

Fig. 4 presents some estimation results from a sample simulation day in Phoenix in May. The day starts with a 7.5 h rest period, which is not shown on the plot. Then there is a short trip and a long rest period until the next trip. This behavior can represent a daily commute to work. After the last trip, the battery is charged until reaching its maximum capacity value, and the vehicle is at rest until the day ends. For this simulation case, air cooling is employed, which is also depicted in the first graph: Whenever the temperature exceeds 35 °C, air cooling kicks in, and temperature starts to drop. The car is assumed to be outside and unplugged during rest periods; therefore the radiation effects are also included in calculating the battery temperature.

3.2. Drive cycle

Fig. 5a shows the degradation profiles of assuming different driving cycles in Phoenix, in the case of no air-cooling. As expected,

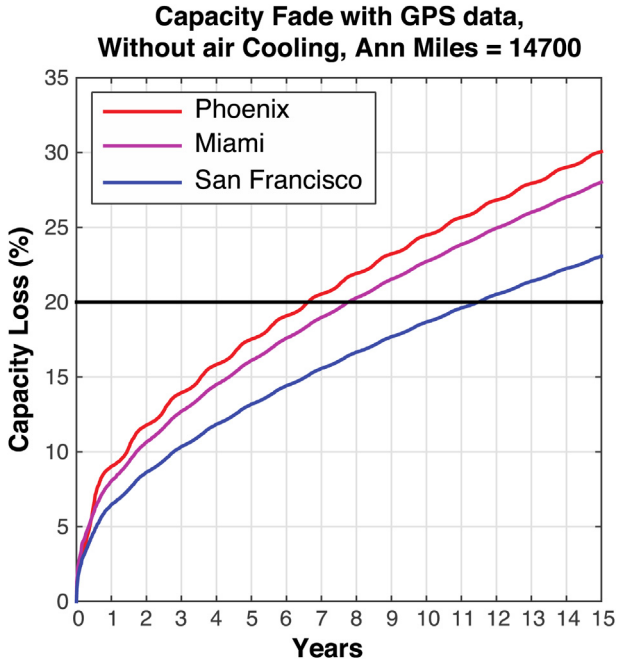

Fig. 6. Capacity fade comparison between cities using GPS data. No air-cooling is employed and total annual miles driven is 14,700 miles.

the US06 drive cycle results in more degradation: battery life is halved compared to the GPS drive cycles (using 20% capacity loss as the end of life criteria). UDDS results are comparable to GPS. UDDS is a milder cycle; however, driving the same distances with UDDS takes considerably longer compared to GPS.

Fig. 5b shows a comparison of the degradation profiles between the two approaches we use to perform simulations with US06 data. As can be seen, assuming the same driving profile every day results in less degradation compared to replacing trips in the GPS.

In both approaches with US06, degradation is very fast, and 20% capacity loss is reached in less than 3 years. To investigate this issue and test any model errors, we perform two additional case studies: In the first case, we test the effect of energy management strategy by assuming a blended mode CD operation. In a blended CD mode operation, instead of behaving like a pure electric vehicle, the PHEV uses a mix of gasoline and electricity until the usable battery charge is depleted. For this case, we perform both CD and CS mode simulations using the Toyota Prius control system model in Simulink described in Section 2.3.1. In the second case, we investigate the pack size implications and perform the simulations again assuming a pack with 5 times more modules with the same cell configurations. As expected, in both cases a significant reduction in capacity fade is observed. With blended mode strategy, the battery life quadruples, as shown in Fig. 5c although this may change the amount of gasoline consumed. In the case of a bigger pack, the degradation rate is slow, and the battery EOL is not reached after fifteen years as depicted in Fig. 5d. These results suggest that the cost of a larger battery pack sized to last the life of the vehicle (with lower current draw and heat generation per cell) could be lower than the cost of an equivalent battery capacity spread over multiple smaller packs replaced over time as each reaches EOL (depending on the pack cost and discount rate) even if the same cells are used. An additional benefit of larger packs is that less-expensive cells can often be used [72]. These results are consistent with the observations that degradation is slower in large battery packs, and small-battery PHEVs in the marketplace are typically designed as blended-operation vehicles rather than EREVs.

3.3. Regional effects

The comparison of capacity fade at three cities is given in Fig. 6. It is observed that, battery life in San Francisco is 75% longer than battery life in Phoenix, mainly because less cabin thermal conditioning use in a mild climate decrease the load on the battery, therefore increasing life. In Miami battery life is one year longer than Phoenix.

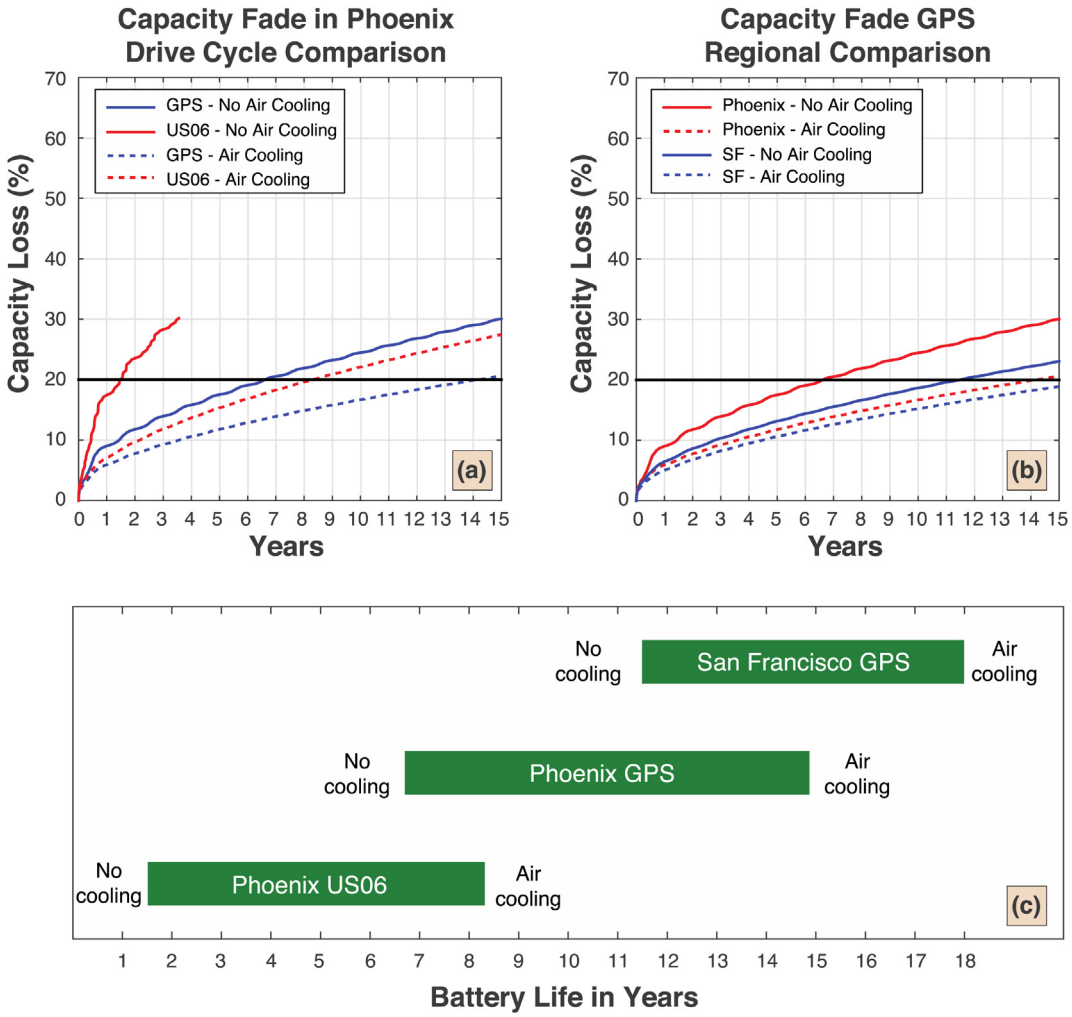

Fig. 7. Effect of air cooling on capacity fade and battery life when annual miles driven are 14,700 miles. **(a)** Capacity Fade in Phoenix, comparison of air cooling vs no cooling for two drive cycles. US06 simulations are performed using Approach 1. **(b)** Capacity Fade in Phoenix and San Francisco, using GPS data. The comparison of air-cooling vs. no cooling is provided for two cities **(c)** Improvement in battery life by air-cooling for different cases simulated. US06 simulations were performed using Approach 1.

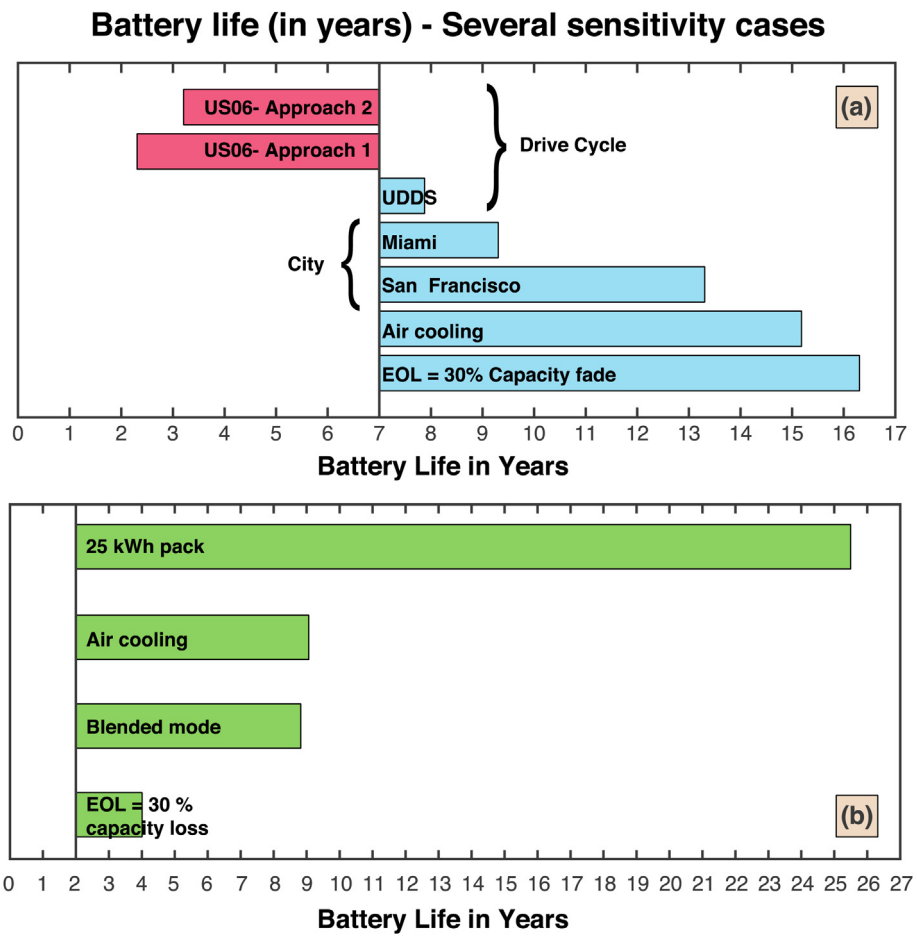

Fig. 8. **(a)** Comparison of battery life for various cases simulated. Vertical line presents the base case (city: Phoenix, drive cycle: GPS, thermal management: none, annual miles driven = 12,400 miles, battery EOL: 20% capacity fade) **(b)** Battery life comparison change for US06 cases simulated at 14,700 miles. Vertical line presents the base case (city: Phoenix, thermal management: none, battery EOL: 20% capacity fade).

3.4. *Effect of thermal management*

Air-cooling can improve battery life significantly. In Phoenix, battery life doubles using the GPS data, and using US06 battery life is almost 8 times as long, as shown in Fig. 7a. The degree of improvement also depends on the city. As Fig. 7b shows, for San Francisco the improvement with air-cooling is less than in Phoenix. It is also observed that, the seasonal variation seen in the rate of capacity loss under no cooling condition disappears and the capacity loss curves become smooth under air-cooling condition. Due to air-cooling, the effect of peak temperatures is reduced, decreasing the change in the capacity loss behavior across seasons. Fig. 7c summarizes the improvement of battery life by air-cooling for the cases simulated.

3.5. *Battery end-of-life criteria*

For all the results discussed so far, the battery's end-of-life (EOL) is assumed to be when it has lost 20% of its capacity. However, individual drivers might continue using their vehicles after this threshold, and with some vehicle designs the driver may not observe any change in range or performance at 20% fade (e.g.: a sufficiently small operational SOC window). As an example, if the battery end-of-life is set to 30% capacity loss, in most of the cases examined the battery life is longer than 15 years.

The change of battery life under various cases compared to base case simulation in Phoenix is summarized in Fig. 8a. In addition, Fig. 8b shows the comparison of different cases that were simulated with a US06 drive cycle.

4. Conclusions

We developed a simulation model of vehicle and battery operations, heat generation, heat transfer, and battery degradation during vehicle operation, charging, and rest to estimate PHEV battery degradation under various scenarios. We use the results to identify key drivers of battery degradation. We estimate for a base case of 12,400 miles per year; driving conditions based on GPS data collected in Atlanta, GA; ambient temperature and solar radiation based on data from Phoenix, AZ; and a 20% capacity fade end-of-life criteria that an EREV PHEV with a 5 kWh Li-ion battery pack composed of cylindrical ANR26650 $LiFePO_4$/Graphite cells manufactured by A123 systems without air cooling has an expected life of seven years. This base case represents a fairly aggressive vehicle design test case, since a relatively small battery pack is being used as the only power source for the PHEV in charge-depleting mode, and we expect that our life estimates are likely optimistic due to some simplifying assumptions such as ignoring temperature gradients among cells in the pack and within each cell. Applying an air cooling system or relaxing the end-of-life criteria to 30% fade can more-than double this life estimate, and driving in a milder climate region can nearly double the life estimate. Milder driving (UDDS)

can increase life slightly, while aggressive driving (US06) can cut life by two thirds. The presence of an air-cooling system reduces the implications of aggressive driving and hot climate, and changing the PHEV to blended operation or increasing the size of the battery pack substantially increase battery life.

Acknowledgements

The authors would like to thank Dr. Kandler Smith from National Renewable Energy Laboratory for his help with the thermal network model as well as his guidance and feedback; Prof. Jay Whitacre from Carnegie Mellon University for his guidance on battery degradation; Prof. Huei Peng from University of Michigan for sharing their model of the Toyota Hybrid Powertrain System; and Hector Perez from University of California, Berkeley for his help with the battery equivalent circuit parameters. This work was funded in part by grants from the Fulbright Program, Toyota Motor Corporation, and the National Science Foundation (CAREER Grant 074791). The views expressed are those of the authors and not necessarily those of the sponsors.

Appendix A. Supplementary data

Supplementary data related to this article can be found at http://dx.doi.org/10.1016/j.jpowsour.2016.10.104.

Nomenclature

Parameter

φ^{GPS}	Travel profile from NHTS
t^{START}	Trip start time, s
t^{END}	Trip end time, s
v^{GPS}	Vehicle speed profile from GPS data, m s^{-1}
t^{CHG}	Charge duration, s
C^{RATED}	Battery rated capacity, Ah
Φ^{SOC}	State-of-charge level
I^{CHG}	Charge current, A
P	Power drawn from battery, W
v	Vehicle speed, m s^{-1}
a	Vehicle acceleration, m s^{-2}
$\Phi^{SOC,MIN}$	Min. SOC level allowed
m^{VEH}	Vehicle, mass kg
C^{DRAG}	Vehicle drag coefficient
A^{FRONT}	Vehicle frontal area, m^2
C^{RR}	Vehicle tire rolling resistance coefficient
η^{RB}	Efficiency of power transfer from regenerative braking to battery
η^{BW}	Efficiency of power transfer from battery to wheels
ρ^{AIR}	Air density, kg m^{-3}
P^{AUX}	Power consumed by auxiliary equipment, W
$N^{CELL,PACK}$	Number of cells per pack
A^{CELL}	Cell surface area, m^2
V^{OCV}	Cell open circuit voltage, V
V	Cell voltage, V
R^{OHM}	Ohmic resistance, Ω
R^{D1}, R^{D2}	Resistances of the RC couples in battery ECM, Ω
C^{D1}, C^{D2}	Capacitances of the RC couples in battery ECM, F
V^{D1}, V^{D2}	Voltages across RC couples in battery ECM, V
t^{S}	Sampling period, s
$\Phi^{SOCINDEX}$	State of charge index for equivalent circuit model look up tables
T^{INDEX}	Temperature index for equivalent circuit model look up tables
T^{BAT}	Battery temperature, °C
M^{CAB}	Vehicle cabin thermal mass, J $°C^{-1}$
M^{BAT}	Battery thermal mass, J $°C^{-1}$
$\dot{Q}^{GEN,BAT}$	Heat generation rate inside the battery, W
$\dot{Q}^{TR}$	Heat transferred to or from the battery, W
I	Current drawn from the battery during driving, Amp
$N^{CELL,PACK}$	Number of cells in the pack
$\dot{Q}^{TR,FC}$	heat transfer by forced air convection, W
$\dot{Q}^{TR,NC}$	heat transferred from the battery to the cabin and outside by natural convection and conduction, W
v^{AIR}	Air speed entering the battery when cooling fan is turned on, m^3 h^{-1}
$N^{CELL,MODULE}$	Number of cells in a module
h	Overall heat transfer coefficient, W K^{-1}
D^{CELL}	Cell diameter, mm
ΔT^{LM}	Log mean temperature difference, °C
L^{CELL}	Cell length, mm
Nu_D	Nusselt number
k^{AIR}	Thermal conductivity of air, W mK^{-1}
$Re_{D,max}$	Reynolds number calculated at max. air velocity
Pr	Prandtl Number
T^{FILM}	Film temperature, °C
T^{SURF}	Surface temperature, °C
T^{AIR}	Air inlet temperature to the battery, °C
T^{AIROUT}	Air outlet temperature from the battery, °C
ρ^{AIR}	Air density, Kg m^{-1}
A^{T}	Air inlet area, mm^2
c^{AIR}	Air constant specific heat, J kgK^{-1}
T^{CAB}	Vehicle cabin temperature, °C
T^{AMB}	Ambient temperature, °C
K^{ab}	thermal resistance between battery and ambient, W K^{-1}
K^{ac}	thermal resistance between cabin and ambient, W K^{-1}
K^{cb}	Thermal resistance relating battery conduction to cabin, W K^{-1}
$\dot{Q}^{CAB}$	Heat transfer rate from the cabin, W
$\dot{Q}^{RAD}$	Radiative heat transfer, W
$\dot{Q}^{HVAC}$	heat removal from the cabin by HVAC system, W
$\dot{q}^{SOLAR}$	global diffuse horizontal radiation per unit area
ε	surface emissivity
A^{CAR}	Car surface area, m^2
θ^{CYC}	percent capacity fade with cycling, %
I^{CELL}	current drawn from (or charged to) the cell, A
C^{CELL}	nominal cell capacity, Ah
R^{GAS}	Universal gas constant
$\phi^{AH,TH}$	ampere-hour (Ah) throughput, Ah
θ^{STO}	capacity loss during storage, %
t^{STO}	Storage duration, days

Indices

k	Travel day
τ	trip
t	Time step

References

[1] J.J. Michalek, M. Chester, P. Jaramillo, C. Samaras, C.-S.N. Shiau, L.B. Lave, Valuation of plug-in vehicle life-cycle air emissions and oil displacement benefits, Proc. Natl. Acad. Sci. U. S. A. 108 (2011) 16554–16558, http://dx.doi.org/10.1073/pnas.1104473108.

[2] T.R. Hawkins, O.M. Gausen, A.H. Strømman, Environmental impacts of hybrid and electric vehicles—a review, Int. J. Life Cycle Assess. 17 (2012) 997–1014, http://dx.doi.org/10.1007/s11367-012-0440-9.

[3] J. Axsen, A. Burke, K.S. Kurani, Batteries for PHEVs: comparing goals and state

of Technology, in: G. Pistoia (Ed.), Electr. Hybrid Veh. Sources, Model. Infrastruct. Mark, Elsevier, 2010, pp. 405–427.
[4] M. Delucchi, T. Lipman, Lifetime cost of battery, fuel-cell, and plug-in hybrid electric vehicles, in: Electr. Hybrid Veh. Sources, Model. Infrastruct. Mark, 2010, pp. 19–60.
[5] T. Markel, A. Brooker, J. Gonder, M.O. Keefe, A. Simpson, M. Thornton, Plug-in Hybrid Vehicle Analysis, Milestone Report, National Renewavke Energy Labratory, 2006.
[6] A. Sakti, J.J. Michalek, E.R.H. Fuchs, J.F. Whitacre, A Techno-economic Analysis and Optimization of Li-ion Batteries for Personal Vehicle Electrification, (n.d.) 1–31.
[7] United States Adv. Batter. Consort, Usabc, Electric Vehicle Battery Test Procedures - Rev. 2, 1996.
[8] C.-S.N. Shiau, N. Kaushal, C.T. Hendrickson, S.B. Peterson, J.F. Whitacre, J.J. Michalek, Optimal plug-in hybrid electric vehicle design and allocation for minimum life cycle cost, petroleum consumption, and greenhouse gas emissions, J. Mech. Des. 132 (2010) 091013, http://dx.doi.org/10.1115/1.4002194.
[9] Idaho National Laboratory, Battery Calendar Life Estimator Manual, 2012. http://avt.inel.gov/battery/pdf/BatteryLifeEstimator.pdf.
[10] A. Pesaran, T. Markel, H. Tataria, D. Howell, Battery Requirements for Plug-in Hybrid Electric Vehicles–analysis and Rationale, 2009. http://www.nrel.gov/docs/fy09osti/42240.pdf (Accessed 12 December 2012).
[11] USABC, USABC Goals for Advanced Batteries for PHEVs for FY 2018 to 2020 Commercialization, MI USABC, Southfield, 2014, p. 2020.
[12] P. a. Nelson, K.G. Gallagher, I. Bloom, D.W. Dees, Modeling the Performance and Cost of Lithium-ion Batteries for Electric-drive Vehicles Chemical Sciences and Engineering Division, 2012.
[13] M. Broussely, Battery requirements for HEVs, PHEVs, and EVs: an overview, in: Electr. Hybrid Veh. Sources, Model. Infrastruct. Mark, 2010, pp. 305–347.
[14] Y. Zhang, C.-Y. Wang, X. Tang, Cycling degradation of an automotive LiFePO4 lithium-ion battery, J. Power Sources 196 (2011) 1513–1520, http://dx.doi.org/10.1016/j.jpowsour.2010.08.070.
[15] K. Amine, J. Liu, I. Belharouak, High-temperature storage and cycling of C-LiFePO/graphite Li-ion cells, Electrochem. Commun. 7 (2005) 669–673, http://dx.doi.org/10.1016/j.elecom.2005.04.018.
[16] D. Li, D. Danilov, Z. Zhang, H. Chen, Y. Yang, P.H.L. Notten, Modeling the SEI-formation on graphite electrodes in LiFePO4 batteries, J. Electrochem. Soc. 162 (2015) A858–A869, http://dx.doi.org/10.1149/2.0161506jes.
[17] R. Deshpande, M. Verbrugge, Y.-T. Cheng, J. Wang, P. Liu, Battery cycle life prediction with coupled chemical degradation and fatigue mechanics, J. Electrochem. Soc. 159 (2012) A1730–A1738, http://dx.doi.org/10.1149/2.049210jes.
[18] J. Groot, M. Swierczynski, A.I. Stan, S.K. Kær, On the complex ageing characteristics of high-power LiFePO4/graphite battery cells cycled with high charge and discharge currents, J. Power Sources 286 (2015) 475–487, http://dx.doi.org/10.1016/j.jpowsour.2015.04.001.
[19] S.B. Peterson, J. Apt, J.F. Whitacre, Lithium-ion battery cell degradation resulting from realistic vehicle and vehicle-to-grid utilization, J. Power Sources 195 (2010) 2385–2392, http://dx.doi.org/10.1016/j.jpowsour.2009.10.010.
[20] J. Wang, P. Liu, J. Hicks-Garner, E. Sherman, S. Soukiazian, M. Verbrugge, et al., Cycle-life model for graphite-LiFePO4 cells, J. Power Sources 196 (2011) 3942–3948, http://dx.doi.org/10.1016/j.jpowsour.2010.11.134.
[21] P. Liu, J. Wang, J. Hicks-Garner, E. Sherman, S. Soukiazian, M. Verbrugge, et al., Aging mechanisms of LiFePO[sub 4] batteries deduced by electrochemical and structural analyses, J. Electrochem. Soc. 157 (2010), http://dx.doi.org/10.1149/1.3294790. A499.
[22] A123 Systems Inc., Development of Battery Packs for Space Applications about A123Systems, 2007.
[23] S. Grolleau, A. Delaille, H. Gualous, P. Gyan, R. Revel, J. Bernard, et al., Calendar aging of commercial graphite/LiFePO4 cell – predicting capacity fade under time dependent storage conditions, J. Power Sources (2013), http://dx.doi.org/10.1016/j.jpowsour.2013.11.098.
[24] Y. Zheng, Y.-B. He, K. Qian, B. Li, X. Wang, J. Li, et al., Effects of state of charge on the degradation of LiFePO4/graphite batteries during accelerated storage test, J. Alloys Compd. 639 (2015) 406–414, http://dx.doi.org/10.1016/j.jallcom.2015.03.169.
[25] A123 Systems Inc., High Power Lithium Ion ANR26650M1A, 2010.
[26] N. Omar, M.A. Monem, Y. Firouz, J. Salminen, J. Smekens, O. Hegazy, et al., Lithium iron phosphate based battery – assessment of the aging parameters and development of cycle life model, Appl. Energy 113 (2014) 1575–1585, http://dx.doi.org/10.1016/j.apenergy.2013.09.003.
[27] H. Song, Z. Cao, X. Chen, H. Lu, M. Jia, Z. Zhang, et al., Capacity fade of LiFePO4/graphite cell at elevated temperature, J. Solid State Electrochem 17 (2012) 599–605, http://dx.doi.org/10.1007/s10008-012-1893-2.
[28] Z. Li, L. Lu, M. Ouyang, Y. Xiao, Modeling the capacity degradation of LiFePO4/graphite batteries based on stress coupling analysis, J. Power Sources 196 (2011) 9757–9766, http://dx.doi.org/10.1016/j.jpowsour.2011.07.080.
[29] M. Broussely, S. Herreyre, P. Biensan, Aging mechanism in Li ion cells and calendar life predictions, J. Power … 98 (2001) 13–21. http://www.sciencedirect.com/science/article/pii/S0378775301007224 (Accessed 12 December 2012).
[30] E. Thomas, I. Bloom, J. Christophersen, V. Battaglia, Statistical methodology for predicting the life of lithium-ion cells via accelerated degradation testing, J. Power Sources 184 (2008) 312–317, http://dx.doi.org/10.1016/j.jpowsour.2008.06.017.
[31] A.A. Pesaran, Battery thermal management, in: Ev And Hevs: Issues And Solutions, Advanced Automotive Battery Conference, Las Vegas, Nevada, February 6–8, 2001, 2001.
[32] S. Chen, C. Wan, Y. Wang, Thermal analysis of lithium-ion batteries, J. Power Sources 140 (2005) 111–124, http://dx.doi.org/10.1016/j.jpowsour.2004.05.064.
[33] C. Forgez, D. Vinh Do, G. Friedrich, M. Morcrette, C. Delacourt, Thermal modeling of a cylindrical LiFePO4/graphite lithium-ion battery, J. Power Sources 195 (2010) 2961–2968, http://dx.doi.org/10.1016/j.jpowsour.2009.10.105.
[34] U. Iraola, I. Aizpuru, J.M. Canales, a Etxeberria, I. Gil, Methodology for Thermal Modelling of Lithium- Ion Batteries, 2013, pp. 6750–6755.
[35] A. Tourani, P. White, P. Ivey, A multi scale multi-dimensional thermo electrochemical modelling of high capacity lithium-ion cells, J. Power Sources 255 (2014) 360–367, http://dx.doi.org/10.1016/j.jpowsour.2014.01.030.
[36] X. Zhang, Thermal analysis of a cylindrical lithium-ion battery, Electrochim. Acta 56 (2011) 1246–1255, http://dx.doi.org/10.1016/j.electacta.2010.10.054.
[37] J. Bakker, Pack Level Design Optimization for Electric Vehicle Thermal Management Systems Minimizing by, 2013.
[38] K. Buford, J. Williams, M. Simonini, Determining Most Energy Efficient Cooling Control Strategy of a Rechargeable Energy Storage System, 2011, http://dx.doi.org/10.4271/2011-01-0893.
[39] D.H. Jeon, S.M. Baek, Thermal modeling of cylindrical lithium ion battery during discharge cycle, Energy Convers. Manag. 52 (2011) 2973–2981, http://dx.doi.org/10.1016/j.enconman.2011.04.013.
[40] X. Li, F. He, L. Ma, Thermal management of cylindrical batteries investigated using wind tunnel testing and computational fluid dynamics simulation, J. Power Sources 238 (2013) 395–402, http://dx.doi.org/10.1016/j.jpowsour.2013.04.073.
[41] K. Yu, X. Yang, Y. Cheng, C. Li, Thermal analysis and two-directional air flow thermal management for lithium-ion battery pack, J. Power Sources 270 (2014) 193–200, http://dx.doi.org/10.1016/j.jpowsour.2014.07.086.
[42] Y.S. Choi, D.M. Kang, Prediction of thermal behaviors of an air-cooled lithium-ion battery system for hybrid electric vehicles, J. Power Sources 270 (2014) 273–280, http://dx.doi.org/10.1016/j.jpowsour.2014.07.120.
[43] T. Wang, K.J. Tseng, J. Zhao, Z. Wei, Thermal investigation of lithium-ion battery module with different cell arrangement structures and forced air-cooling strategies, Appl. Energy 134 (2014) 229–238, http://dx.doi.org/10.1016/j.apenergy.2014.08.013.
[44] H. Park, A design of air flow configuration for cooling lithium ion battery in hybrid electric vehicles, J. Power Sources 239 (2013) 30–36, http://dx.doi.org/10.1016/j.jpowsour.2013.03.102.
[45] N. Yang, X. Zhang, G. Li, D. Hua, Assessment of the forced air-cooling performance for cylindrical lithium-ion battery packs: a comparative analysis between aligned and staggered cell arrangements, Appl. Therm. Eng. 80 (2015) 55–65, http://dx.doi.org/10.1016/j.applthermaleng.2015.01.049.
[46] O. Gross, S. Clark, Optimizing electric vehicle battery life through battery thermal management, Gener. J. Am. Soc. Aging (2011), http://dx.doi.org/10.4271/2011-01-1370.
[47] K. Smith, M. Earleywine, E. Wood, Comparison of plug-in hybrid electric vehicle battery life across geographies and drive cycles, SAE Tech. (2012). http://www.nrel.gov/vehiclesandfuels/energystorage/pdfs/53817.pdf (Accessed 15 December 2012).
[48] J. Neubauer, E. Wood, Thru-life impacts of driver aggression, climate, cabin thermal management, and battery thermal management on battery electric vehicle utility, J. Power Sources 259 (2014) 262–275, http://dx.doi.org/10.1016/j.jpowsour.2014.02.083.
[49] http://www.nrel.gov/vehiclesandfuels/secure_transportation_data.html, NREL: Vehicles and Fuels Research - Secure Transportation Data Center, (n.d.). http://www.nrel.gov/vehiclesandfuels/secure_transportation_data.html.
[50] E. Traut, C. Hendrickson, E. Klampfl, Y. Liu, J.J. Michalek, Optimal design and allocation of electrified vehicles and dedicated charging infrastructure for minimum life cycle greenhouse gas emissions and cost, Energy Policy 51 (2012) 524–534, http://dx.doi.org/10.1016/j.enpol.2012.08.061.
[51] U.S. Department of Transportation Federal Highway Administration, Highway Statistics Series, Highway Statistics 2011: Annual Vehicle Distance Traveled in Miles and Related Data – 2011 By Highway Category and Vehicle Type, Available at: http://www.fhwa.dot.gov/policyinformation/statistics/2011/pdf/vm1.pdf.
[52] U. EPA, Dynamometer Drive Schedules | Testing and Measuring Emissions |US EPA, (n.d.). http://www.epa.gov/nvfel/testing/dynamometer.htm (Accessed 29 December 2013).
[53] Hymotion ™ L5 Plug-in Conversion Module Upgrade Your PRIUS to a Plug-in Hybrid Now and Get, 2009.
[54] J. Liu, H. Peng, Modeling and control of a power-split 16 (2008) 1242–1251.
[55] J. Liu, H. Peng, Z. Filipi, Modeling and Analysis of the Toyota hybrid System, 2005, pp. 24–28.
[56] Y. Ma, H. Teng, M. Thelliez, Electro-thermal modeling of a lithium-ion battery system, SAE Int. J. Engines 3 (2010) 306–317.
[57] H.E. Perez, J.B. Siegel, X. Lin, A.G. Stefanopoulou, Y. Ding, M.P. Castanier, Parameterization and validation of an integrated electro-thermal cylindrical LFP battery model 3 (2012) 41–50, http://dx.doi.org/10.1115/DSCC2012-MOVIC2012-8782. Renew. Energy Syst. Robot. Robust Control. Single Track Veh. Dyn. Control. Stoch. Model. Control Algorithms Robot. Struct. Dyn. Smart

Struct.
[58] DeepBlue, (n.d.). http://deepblue.lib.umich.edu/handle/2027.42/97341.
[59] R.C. Kroeze, P.T. Krein, Electrical battery model for use in dynamic electric vehicle simulations, 2008, IEEE Power Electron. Spec. Conf. (2008) 1336–1342, http://dx.doi.org/10.1109/PESC.2008.4592119.
[60] L. Lam, P. Bauer, E. Kelder, A practical circuit-based model for Li-ion battery cells in electric vehicle applications, 2011, IEEE 33rd Int. Telecommun. Energy Conf. (2011) 1–9, http://dx.doi.org/10.1109/INTLEC.2011.6099803.
[61] H.E. Perez, J.B. Siegel, A.G. Stefanopoulou, in: JSME 2012 11th Motion and Vibration Conference Electro-Thermal Cylindrical LFP Battery Model, 2012, pp. 1–10.
[62] M. Muratori, N. Ma, M. Canova, Y. Guezennec, A 1+1D thermal dynamic model of a LI-ion battery cell, in: Proc. ASME Dyn. Syst. Control Conf., Cambridge, Massachusetts, 2010, pp. 625–631.
[63] G. Zhang, L. Cao, S. Ge, C. Wang, Situ measurement of Li-Ion battery internal temperature, Meet. Abstr. 536 (2013) 2013. https://ecs.confex.com/ecs/224/webprogram/Abstract/Paper25308/B3-0538.pdf (Accessed 13 January 2014).
[64] Y. Ye, Y. Shi, L.H. Saw, A. a. O. Tay, An electro-thermal model and its application on a spiral-wound lithium ion battery with porous current collectors, Electrochim. Acta (2014), http://dx.doi.org/10.1016/j.electacta.2013.12.122.
[65] Y. Zheng, M. Ouyang, L. Lu, J. Li, Understanding aging mechanisms in lithium-ion battery packs: from cell capacity loss to pack capacity evolution, J. Power Sources 278 (2015) 287–295, http://dx.doi.org/10.1016/j.jpowsour.2014.12.105.
[66] K. Chiu, C.-H. Lin, S. Yeh, Y. Lin, C. Huang, K. Chen, Cycle life analysis of series connected lithium-ion batteries with temperature difference, J. Power Sources 263 (2014) 75–84, http://dx.doi.org/10.1016/j.jpowsour.2014.04.034.
[67] K. Smith, A. Le, L. Chaney, NREL_PriusThermModel_xEV, (n.d.).
[68] M. Zolot, A. Pesaran, M. Mihalic, Thermal evaluation of Toyota Prius battery pack, Futur. Conf. (2002). http://www.nrel.gov/vehiclesandfuels/energystorage/pdfs/2a_2002_01_1962.pdf (Accessed 12 December 2012).
[69] A123 Hymotion Animation, 2010. https://www.youtube.com/watch?v=5APr9sM3fVw.
[70] F.P. Incropera, D.P. DeWitt, Fundamentals of Heat and Mass Transfer, 1996.
[71] National Solar Radiation Data Base: 1991-2005 Update: TMY3, (n.d.). http://rredc.nrel.gov/solar/old_data/nsrdb/1991-2005/tmy3/(accessed April 16, 2014).
[72] A. Sakti, J.J. Michalek, E. Fuchs, J. Whitacre, A techno-economic analysis and optimization of Li-ion batteries for light-duty passenger vehicle electrification, J. Power Sources (2014).